APL Photonics

Invited Article: Topological crystalline protection in a photonic system

Cite as: APL Photonics 1, 050803 (2016); https://doi.org/10.1063/1.4953364
Submitted: 15 March 2016 • Accepted: 24 May 2016 • Published Online: 06 July 2016

Jian-Xiao Zhang, Mikael C. Rechtsman and Chao-Xing Liu

openaccess

View Online Export Citation CrossMark

ARTICLES YOU MAY BE INTERESTED IN

Nonlinear topological photonics
Applied Physics Reviews 7, 021306 (2020); https://doi.org/10.1063/1.5142397

A perspective on topological nanophotonics: Current status and future challenges
Journal of Applied Physics 125, 120901 (2019); https://doi.org/10.1063/1.5086433

A Topological Look at the Quantum Hall Effect
Physics Today 56, 38 (2003); https://doi.org/10.1063/1.1611351

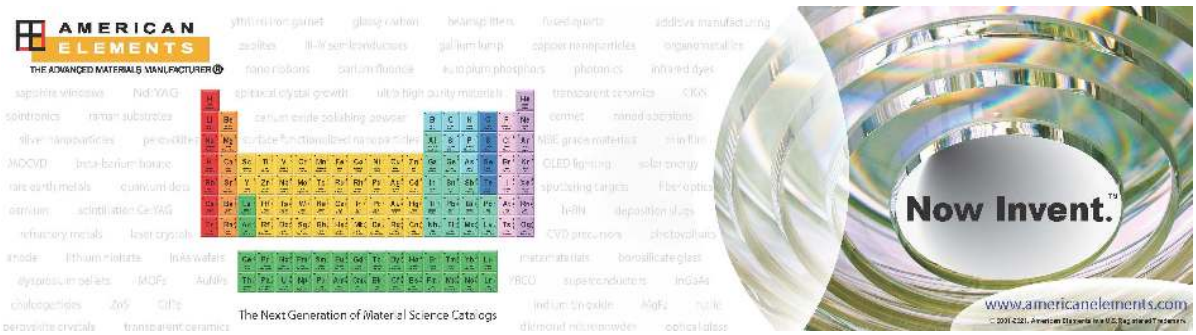

AIP Publishing

© 2016 Author(s).

Invited Article: Topological crystalline protection in a photonic system

Jian-Xiao Zhang, Mikael C. Rechtsman, and Chao-Xing Liu
Department of Physics, The Pennsylvania State University, University Park, Pennsylvania 16802-6300, USA

(Received 15 March 2016; accepted 24 May 2016; published online 6 July 2016)

Topological crystalline insulators are a class of materials with a bulk energy gap and edge or surface modes, which are protected by crystalline symmetry, at their boundaries. They have been realized in electronic systems: in particular, in SnTe. In this work, we propose a mechanism to realize photonic boundary states topologically protected by crystalline symmetry. We map this one-dimensional system to a two-dimensional lattice model with opposite magnetic fields, as well as opposite Chern numbers in its even and odd mirror parity subspaces, thus corresponding to a topological mirror insulator. Furthermore, we test the robustness of the boundary modes depending on their mirror parity by performing time dependent evolution simulations in a photonic setting with realistic experimental parameters. © *2016 Author(s). All article content, except where otherwise noted, is licensed under a Creative Commons Attribution (CC BY) license (http://creativecommons.org/licenses/by/4.0/).* [http://dx.doi.org/10.1063/1.4953364]

INTRODUCTION

Topological insulators represent a novel quantum state of matter: they behave as insulators in their interior (meaning they have a bulk band gap), but have ungapped surface/edge states at their terminations. These states are "protected" in the sense that they must exist despite the presence of defects or disorder, and under certain conditions give rise to scatter-free robust transport. The early study of topological states was focused on electronic systems, but recently the realization by Haldane and Raghu[1,2] that gyromagnetic photonic crystals could exhibit non-trivial topological invariants opened the door to the new field of "topological photonics"[3] in which the propagation of photons in a dielectric structure is protected in a similar sense to electrons in a crystal lattice. The first experimental realization of this phenomenon was made in the group of Soljačić[4,5] for the regime of microwave photons. However, scaling the wavelength down to the optical regime (in order to realize topological states in optical devices) was not possible using a similar mechanism due to weak magnetic response in that frequency regime. Other mechanisms were proposed,[6–10] and finally experimental demonstrations were made[11] in a system based on evanescently coupled helical waveguides; as well as in two-dimensional coupled ring resonators.[12] While photonic topological protection is conceptually similar to that of electronic topological protection (after all, this phenomenon comes down to non-interacting wave dynamics), photonics offers unique advantages and potential applications. To name a few examples, photonic systems can be designed directly by fabrication (allowing any desired lattice structure to be realized); experiments can be carried out at room temperature, meaning any emergent devices can be brought to application more realistically than those that require very low temperatures; and the robustness associated with topological protection could be of use in an array of devices that rely on the flow of light (e.g., sensors, optical interconnects, electro-optic modulators, isolators, among others).

The use of symmetry has been theoretically proposed as a mechanism to protect new topological states, ever since the discovery of time-reversal invariant topological insulators,[13–21] in which time-reversal symmetry plays an essential role. A large variety of symmetry-protected topological states has been identified theoretically for different symmetry classes and dimensions.[22,23] In contrast, the corresponding material realization in experimentally feasible systems of these new topological states has been limited to only several symmetry classes, mainly for time-reversal

 © Author(s) 2016.

invariant topological insulators,[24–32] the quantum anomalous Hall insulators,[33,34] topological superconductors,[35–40] and topological mirror insulators.[41–46] Therefore, searching for new topological systems for symmetry protected topological states is important for the development of this field.

Topological crystalline insulator (TCI) phases,[41] topological phases that are protected by crystalline symmetry, can exist in a large number of crystal structures with different space group symmetries. A classification of TCIs in different point symmetry groups and space symmetry groups has recently been the focus of much research.[43–50] Compared to quantum spin-Hall-type topological insulators, which can only occur for spinful fermions, topological crystalline insulators can exist in both fermionic and bosonic systems. Therefore, it is natural to ask if one can realize a topological crystalline insulator phase in photonic systems. Indeed, very recently a prediction was made that topological photonic crystals with surface states protected by the glide symmetry could be realized for microwave photons[51] in a macroscopic ferrimagnetic structure.

In this work, we propose the optical realization of crystalline symmetry protected boundary modes in an optical system. The system is quasi-one-dimensional, where an auxiliary parameter, ϕ, of which the Hamiltonian is a function, is used in place of a second spatial dimension. This is reminiscent of Ref. 52, in which a family of one-dimensional systems (defined by a pump parameter) was used to realize a photonic topological edge state and pump that are mapped to the integer quantum Hall effect. We note that another work[53] has predicted an analogue of a quantum spin Hall system that requires C_6 crystalline symmetry; however the edge always breaks that symmetry and so the topological edge states are not protected (and are gapped). The realization of crystalline symmetry protected topological states in the optical regime would allow for a novel paradigm in exploring topological crystalline phases, opening up the possibility to explore the relationship between topological photonic systems and nonlinear/interacting bosonic systems and quantum optical effects such as multi-photon quantum walks.[54]

TIGHT-BINDING MODEL

We start from a simple tight-binding model to illustrate our main idea and then simulate the system in a more realistic situation. We consider a quasi-one-dimensional (1D) chain along the x direction with each unit cell consisting of four sites, denoted by $\alpha = 1,\ldots,4$, as marked by "a" in Fig. 1(a). The positions of the four sites are chosen to preserve y-directional mirror symmetry with respect to the line denoted by "b" in Fig. 1(a). Each site corresponds to a single-mode waveguide. We denote these states as $|s_\alpha\rangle$, and the corresponding creation and annihilation operators as $c_\alpha^\dagger$ and c_α, respectively. Thus, the tight-binding Hamiltonian for this system is given by

$$H = \sum_{\alpha\beta,m} \left[c_m^{\alpha\dagger} \hat{V}_m^{\alpha\beta} c_m^\beta + \left(c_m^{\alpha\dagger} \hat{T}_m^{\alpha\beta} c_{m+1}^\beta + \text{h.c.} \right) \right], \tag{1}$$

where $\alpha,\beta = 1,\ldots,4$ and $m = 1,2,\ldots,M$ denoting the unit cell index. $\hat{V}_m$ describes the on-site energy and the hopping between sites within the mth unit cell. $\hat{T}_m$ describes the hopping between two nearest neighbor unit cells m and $m+1$. In the $\{|s_\alpha\rangle\}$ basis, the Hamiltonians $\hat{V}_m$ and $\hat{T}_m$ are given by

$$\hat{V}_m = \begin{pmatrix} V_m & \gamma_x & 0 & \gamma_y \\ \gamma_x & V_m & \gamma_y & 0 \\ 0 & \gamma_y & V_m & \gamma_x \\ \gamma_y & 0 & \gamma_x & V_m \end{pmatrix}, \qquad \hat{T}_m = \begin{pmatrix} 0 & t & t' & 0 \\ 0 & 0 & 0 & 0 \\ 0 & 0 & 0 & 0 \\ 0 & t' & t & 0 \end{pmatrix}, \tag{2}$$

where $V_m(\phi)$ is the on-site energy of each site in the mth unit cell, chosen to be identical. The parameters γ_x and γ_y denote the hopping between two sites along the x and y directions within one unit cell, as shown in Fig. 1(a). t and t' are hopping parameters between two sites in two unit cells. t corresponds to the $2-1'$ style hopping and t' corresponds to the $2-4'$ style hopping, as labeled in Fig. 1(a). We note that one-dimensional "Shockley" edge states were previously observed in Ref. 55. Note that one-dimensional topological states have been studied in other contexts as well in Refs. 56–59.

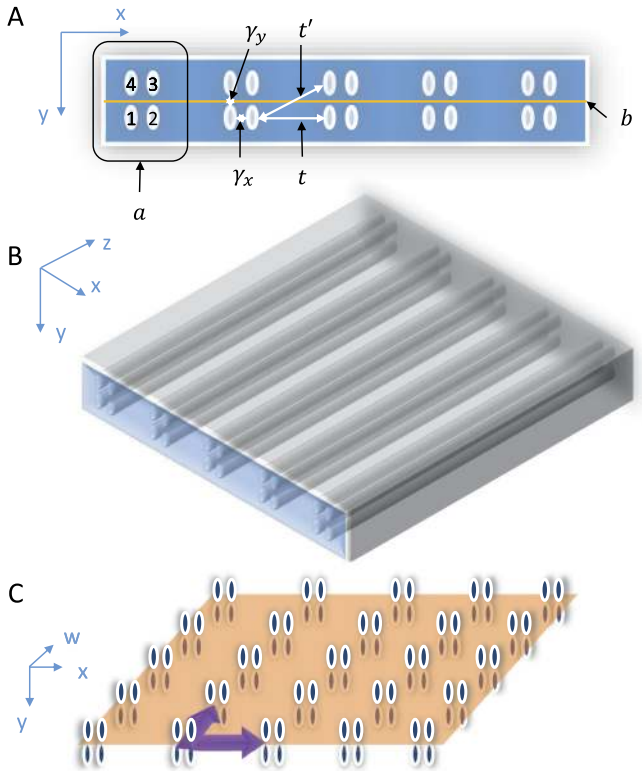

FIG. 1. (a) Schematics for the quasi-1D chain model. There are four confining potentials, denoted by $1,\ldots,4$, in one unit cell, labeled by "a." Four sites in one unit cell are symmetric with respect to the mirror line "b." The intra-unit-cell hoppings are labeled γ_y and γ_x. The inter-unit-cell hoppings are labeled t' and t, respectively. (b) Schematics for the 3D visualization of the waveguide chain. The light propagates along z direction. (c) Schematics of the quasi-2D lattice model which can be mapped from the 1D model. The mirror plane $y=0$ (orange) is parallel with the $x-w$ plane. The complex hopping terms along the x and w directions between unit cells are symbolized by purple arrows. w is conjugate with the parameter θ. (See Hamiltonian Eq. (6).)

The above Hamiltonian preserves the y mirror operator $\hat{M}_y$, given by

$$\hat{M}_y = \begin{pmatrix} 0 & 0 & 0 & 1 \\ 0 & 0 & 1 & 0 \\ 0 & 1 & 0 & 0 \\ 1 & 0 & 0 & 0 \end{pmatrix}, \tag{3}$$

which interchanges the sites 1 and 4 (2 and 3). We set $V_m(\phi) = V_0 + \eta_m(\phi)$, $\gamma_x = \gamma_{x0}$, and $\gamma_y(\phi) = \gamma_{y0} + \delta_m(\phi)$. The parameter ϕ is also known as the pump parameter. By mapping the model into a 2D topological mirror insulator, ϕ plays the role of momentum in the artificial dimension. (See supplementary material[60] for the derivation.)

Let us neglect t, t', η_m, and δ_m, and set $\gamma_{x0} = \gamma_{y0} = \gamma_0$ for the moment. In this limit, the Hamiltonian $\hat{V}_m$ in (Eq. (2)) can be diagonalized and the eigenenergies of the four eigenstates are shown in Fig. 2. We find that two degenerate states $|\psi_+\rangle$ and $|\psi_-\rangle$ with eigenenergy V_0 are well separated from the other two states $|\psi_t\rangle$ and $|\psi_b\rangle$ with energies $V_0 \mp 2\gamma_0$, where we use + (−) to represent odd (even) mirror parity of $\hat{M}_y$. The reason to use 4 sites instead of 2 is to make the ψ_+ and ψ_- degenerate and with opposite mirror parities. This also allows us to show that when we break mirror parity, this degeneracy lifts and topological protection is broken.

In the limit $\eta_m, \delta_m, t, t' \ll V_0, \gamma_0$, we can focus on two degenerate eigenstates $|\psi_+\rangle$ and $|\psi_-\rangle$, and project the total Hamiltonian onto the subspace spanned by these two states. We should note that setting up such a limit is only for separating the other two unnecessary bands. This limitation and projection process will not change the topological properties.

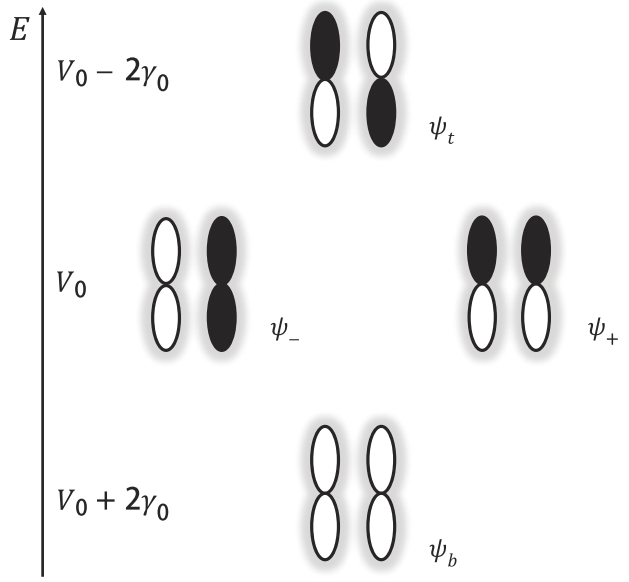

FIG. 2. The eigenenergies and eigenstates for the Hamiltonian in one unit-cell with four sites. White and black colors indicate the sign for the real part of the four different eigenstates.

The eigenstates of two degenerate states are given by $|\psi_+\rangle = \frac{1}{2}(+|s_1\rangle + |s_2\rangle - |s_3\rangle - |s_4\rangle)$, $|\psi_-\rangle = \frac{1}{2}(+|s_1\rangle - |s_2\rangle - |s_3\rangle + |s_4\rangle)$, and let us denote $d_{\pm,m}$ and $d^\dagger_{\pm,m}$ to be the annihilation and creation operators for the states $|\psi_\pm\rangle$ on the mth unit cell, respectively. The effective Hamiltonian after projection is given by

$$H = \sum_{\pm,m} t_{\pm,m}(d^\dagger_{\pm,m}d_{\pm,m+1} + \text{h.c.}) + V_{\pm,m}d^\dagger_{\pm,m}d_{\pm,m}, \tag{4}$$

where the summation $\pm$ is over the parity subspaces. The parameters $t_{\pm,m}$ and $V_{\pm,m}$ are related to the original parameters t, t', δ_m, and V_m by $V_{\pm,m} = V_0 + \eta_m \mp \delta_m$ and $t_\pm = (-t' \pm t)/2$. If we choose $\eta_m = \lambda\cos\phi\cos(2\pi b(m+m_0))$, $\delta_m = \lambda\sin\phi\sin(2\pi b(m+m_0))$, we find $V_\pm = V_0 + \lambda\cos(\phi \pm 2\pi b(m+m_0))$ correspondingly. As a result, the Hamiltonian (Eq. (4)) is nothing but two copies of the Aubry-Andre-Harper (AAH) Hamiltonian[52,61,62] with the effective flux strength b and $-b$ in the odd and even subspaces, respectively. Here m_0 shifts the index of the first unit cell. As a consequence of opposite mirror parities under $\hat{M}_y$, these two copies of the Hamiltonian are decoupled from each other once mirror symmetry $\hat{M}_y$ is preserved. It has been shown that by correctly choosing parameters, boundary modes can exist at the end of a finite chain described by the AAH model, within a fractal set of band gaps.[63] Thus, we perform a direct calculation of the energy spectrum of a finite chain for the model (Eq. (1)).

Here for demonstration, we choose the parameters to be $\gamma_0 = -0.3$ mm^{-1}, $\lambda = 0.1$ mm^{-1}, $t = -0.11$ mm^{-1}, $t' = -0.033$ mm^{-1}, $V_0 = -0.8$ mm^{-1}, $M = 103$, $m_0 = 9$, and $b = \sqrt{5}$. (The unit of energy here is chosen such that it could be reproduced later in the continuum model.) An extra offset between γ_x and γ_y is set by taking $\gamma_{x0} = \gamma_0 + 0.025$ mm^{-1} and $\gamma_{y0} = \gamma_0$. This offset shifts the relative energy level for odd and even bands, in order to emphasize the crossings of edge states inside the mini-gap described later. The four energy levels in one unit cell $|\psi_+\rangle$, $|\psi_-\rangle$, $|\psi_t\rangle$, and $|\psi_b\rangle$ expand into four energy bands as a function of the parameter ϕ, as shown in Fig. 3(a). The $|\psi_+\rangle$ and $|\psi_-\rangle$ bands overlap with each other in the energy regime $[V_0 - \lambda, V_0 + \lambda]$ to the lowest order approximation, which is about $[-1.0\text{ mm}^{-1}, -0.6\text{ mm}^{-1}]$ for the parameters listed above. Each band is split into several sub-bands with mini-gaps. We focus on the mini-gap in the energy range $[-0.73\text{ mm}^{-1}, -0.67\text{ mm}^{-1}]$ denoted as in Fig. 3(a). There are other mini-gaps, for example, in the range of $[-0.95\text{ mm}^{-1}, -0.90\text{ mm}^{-1}]$ and $[-1.32\text{ mm}^{-1}, -1.25\text{ mm}^{-1}]$. Here we show the zoomed-in spectrum in Fig. 3(b) of the mini-gap region "a." We find four energy levels in the mini-gap, denoted by $|\psi_{L+}\rangle$, $|\psi_{R-}\rangle$, $|\psi_{R+}\rangle$, and $|\psi_{L-}\rangle$, or "b," "c," "d," and "e" in Fig. 3(b), respectively, where

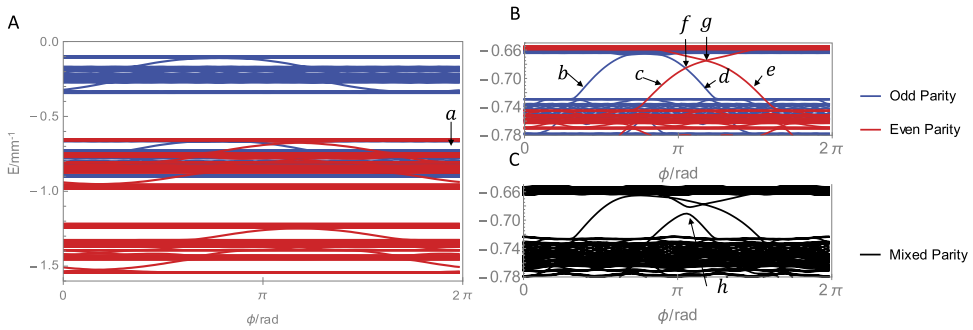

FIG. 3. (a) Energy spectrum for a finite chain ($M = 103, m_0 = 9$) of our tight-binding model. Blue and red colors represent odd and even mirror parities of eigen-wavefunctions, respectively. There are four bands in energy spectrum. The top and bottom bands come from the states $|\psi_t\rangle$ and $|\psi_b\rangle$, while two bands in the energy range $[-1.0\ \text{mm}^{-1}, -0.6\ \text{mm}^{-1}]$ originate from the states $|\psi_\pm\rangle$. A mini-gap, as indicated by "a," exists within the $|\psi_\pm\rangle$ bands. (b) Zoomed-in graph of energy spectrum around the energy range $[-0.78\ \text{mm}^{-1}, -0.66\ \text{mm}^{-1}]$. Boundary modes $|\psi_{L+}\rangle$, $|\psi_{R-}\rangle$, $|\psi_{R+}\rangle$, and $|\psi_{L-}\rangle$, as indicated by "b," "c," "d," and "e," are found within the mini-gap "a." "f" ("g") denotes the crossing between "c" and "d" ("c" and "e"). The light red and light blue shading indicate the mini-gap region "a" of the two corresponding parities. (c) A gap opening for the crossing "f" can be induced by a mirror-symmetry-breaking term ΔH, leading to an anti-crossing "h."

L and R denote the position where the wave function of the state is localized in the chain, and ± indicates the parity of the boundary modes, shown by blue (odd) and red (even) in Fig. 3(b). A more realistic calculation of the wave function in this system will be given in the section titled "Numerical simulations for photonic systems," based on simulating the full continuum problem. The crossing between the boundary modes $|\psi_{R-}\rangle$ and $|\psi_{R+}\rangle$, marked by "f" in Fig. 3(b), is topologically protected due to opposite mirror parities between them, while the crossing between $|\psi_{L-}\rangle$ and $|\psi_{R-}\rangle$, marked by "g" in Fig. 3(b), is gapless because these two states are located at opposite boundaries of the chain. As long as the chain size is large compared with the penetration length of boundary mode, which is around twice the lattice constant for the parameters listed above, the overlapping between wavefunctions at opposite boundaries is negligible.

We test the symmetry protection by adding a mirror-symmetry breaking term ΔH onto $\hat{V}_m$, where

$$\Delta H = \begin{pmatrix} 0 & \Delta & 0 & 0 \\ \Delta & 0 & 0 & 0 \\ 0 & 0 & 0 & -\Delta \\ 0 & 0 & -\Delta & 0 \end{pmatrix} \tag{5}$$

and $\Delta = 0.04$, we find a gap opening between two boundary modes ψ_{R-} ("c") and ψ_{R+} ("d"), as marked by "h" in Fig. 3(c). Thus, we conclude that these boundary modes are stable only when mirror symmetry is present in the system (Eq. (1)).

We would like to emphasize that although our model is written in one dimension, it can be mapped to a two-dimensional (2D) lattice model with complex hopping terms, corresponding to a 2D topological mirror insulator. This is a similar mapping as that made in Ref. 52. We may introduce a fictitious dimension w and extend our 1D tight-binding model to the $x - w$ plane, forming a 2D square lattice as shown in Fig. 1(c). Similar to the unit cell defined in the 1D model, each unit cell at the integer coordinates (x, w) consists of 4 sites, each having one state described by the creation operators $c^{\alpha\dagger}_{x,w}$ where $\alpha = 1, \ldots, 4$. The 2D Hamiltonian can be written as

$$H = \sum_{xw,\alpha\beta} \left[\left(c^{\alpha\dagger}_{x,w+1} \hat{T}^{\alpha\beta}_x c^{\beta}_{x,w} + c^{\alpha\dagger}_{x,w+1} \hat{T}^{\alpha\beta}_w c^{\beta}_{x,w} \right) + \text{h.c.} \right] + \sum_{xw,\alpha\beta} \hat{U}_{\alpha\beta} c^{\alpha\dagger}_{x,w} c^{\beta}_{x,w}, \tag{6}$$

where $\hat{T}_{x(w)}$ is the hopping matrix between sites labeled by $\alpha, \beta = 1, 2, 3, 4$, in the adjacent unit cells along the x (w) direction, and $\hat{U}$ is the hopping matrix among sites in one unit cell. The detailed forms of $\hat{T}_{x(w)}$ and $\hat{U}$ are given in the supplementary material.[60]

This Hamiltonian is also invariant under the mirror operation $\hat{M}_y$ (Eq. (3)) about the $x-w$ plane. We define the basis creation operators $d^\dagger_\pm$ in the same way as in Eq. (4) where $\pm$ are defined for the subspaces with odd and even mirror parities as before. Following the same logic from Eq. (1) to Eq. (4), we project the Hamiltonian into the basis of even and odd parity eigenstates. In this new basis, the Hamiltonian takes the form

$$H = \sum\nolimits_{\pm,xw} \left[V_0 d^\dagger_{\pm,xw} d_{\pm,xw} + \left((-t' \pm t) d^\dagger_{\pm,x+1,w} d_{\pm,x,w} + \frac{\lambda}{2} e^{\pm i\theta} d^\dagger_{\pm,x,w+1} d_{\pm,xw} + \text{h.c.} \right) \right], \quad (7)$$

where the parameter $\theta = 2\pi bx$ represents the phase shift during the hopping along the w direction. We notice that the form of θ corresponds to the Landau gauge for a magnetic field with the flux b in one unit cell. Thus, a Chern number can be defined in each mirror subspace for a non-zero b. (See the supplementary material[60] for a topological invariant.) The opposite signs for the phase shift in the mirror even and odd subspaces indicate that the total Chern number is canceled for the whole system. However, a mirror Chern number, as defined in the supplementary material,[60] can characterize non-trivial topological property of our 2D system.[44,52] Therefore, this mapping suggests that our tight-binding model provides a realization of 2D topological mirror insulators.

NUMERICAL SIMULATIONS FOR PHOTONIC SYSTEMS

We have now established topological mirror insulator phases in our simple 1D AAH type of tight-binding model and its mapping to 2D topological mirror insulators is also illustrated above. The realization of this model in a photonic system requires more sophisticated numerical simulation, which includes continuum degrees of freedom and are based on Maxwell's equations. Next, we describe the detailed experimental setup and perform a numerical simulation of photonic lattice systems.

To realize the tight-binding model in a realistic photonic system, we consider an array of evanescently coupled elliptical waveguides in fused silica glass. The difference in refractive index inside and outside the waveguide is utilized to confine the light in the $x-y$ plane and serve as a potential well, as shown in Fig. 1(b). We follow the standard paraxial approximation for this type of waveguides, in which the Maxwell's equation of light can be simplified to a Schrödinger-type equation, namely,

$$i\partial_z \psi(x,y;z) = -\frac{1}{2k_0}(\partial_x^2 + \partial_y^2)\psi(x,y;z) - \frac{k_0 \Delta n(x,y;z)}{n_0}\psi(x,y;z), \quad (8)$$

where ψ is the envelope function of electric fields, k_0 is the wavenumber of ambient light in the medium, n_0 and Δn are respectively the background and the waveguide deviation from background refraction index. In comparison with the Schrödinger equation, one can see that the z direction can be regarded as time. Therefore, the diffraction of light through the waveguides is equivalent to the time evolution of a particle in a potential determined by $-\Delta n(x,y;z)$. This equation has been utilized to describe other topological phases in photonic lattices,[11] as well as a wide variety of effects in linear and nonlinear optics,[64] including (but not limited to) the prediction[65] and observation[66,67] of lattice solitons, stable photorefractive solitons; Anderson localization in optics;[68] conical diffraction;[69] and optical pseudomagnetism.[70] The waveguides used in this work can potentially be fabricated using the femtosecond direct laser writing technique; and are inspired by those described in Ref. 71.

As shown in Fig. 1(b), four elliptical waveguides reside on the corners of a rectangle to simulate one unit cell in our tight-binding model. We place these unit cells one by one to form a chain, as described in the tight-binding model. The confining potential is provided by the deviation of the refraction index inside the waveguides from the background, $V = (\omega/c)\Delta n$, and the hopping term is determined by the overlap between two nearby sites, which can be controlled by adjusting the distance between them. The details of the relation between distance of different sites and energy level positions are described in supplementary material[60] in which we found that we can neglect the off-diagonal hopping term between the sites 1 and 3 (2 and 4) and obtain the Hamiltonian Eq. (2). By carefully controlling the distance between different sites, four elliptical waveguides in one unit cell can indeed reproduce four eigenstates with the desired energy levels as in our tight-binding model.

The energy spectrum of both continuum and tight-binding modes reveals a sub-band structure with mini-band gaps for both parity bands. The validation of tight-binding approximation and a detailed comparison between the spectrum of the continuum model and the tight-binding model are discussed in supplementary material.[60] In short, we find that the dispersion from the continuum model agrees well with that from the tight-binding model. For both the bands with even (red color) and odd (blue color) parities, they are split into three mini-bands, separated by mini-gaps. We can establish the relation between the parameters described in the tight-binding model and the realistic parameters in the continuum simulation model. The parameter ϕ enters through the argument of both V_m and γ_y, which is translated into the variation of refractive index and the separation between waveguides in the continuum model and the experimental setup. This provides a clear roadmap of implementing such artificial dimension momentum in realistic systems.

We next discuss our numerical simulation of the energy spectrum for a waveguide chain with the number of unit cells $M = 23$. The energy spectrum is shown in Figs. 4(a) and 4(c) for two waveguide chains with different parameter sets. For simplicity, we label the waveguide chain for the energy spectrum in Figs. 4(a) and 4(c) as number I and II, respectively, as listed in Table I. Within the tight-binding approximation, the only difference between waveguide chains is the starting index m_0, which is defined in $V_{\pm,m}$ after Eq. (4) and whose importance is described in the supplementary material.[60] It is proven that introducing such shift does not change the topological properties of the system,[52] but only the position of boundary modes in the energy spectrum. We can further map the parameters listed in Table I in tight-binding model to those in continuum model. The comparison between these two models is discussed in detail in the supplementary material.[60]

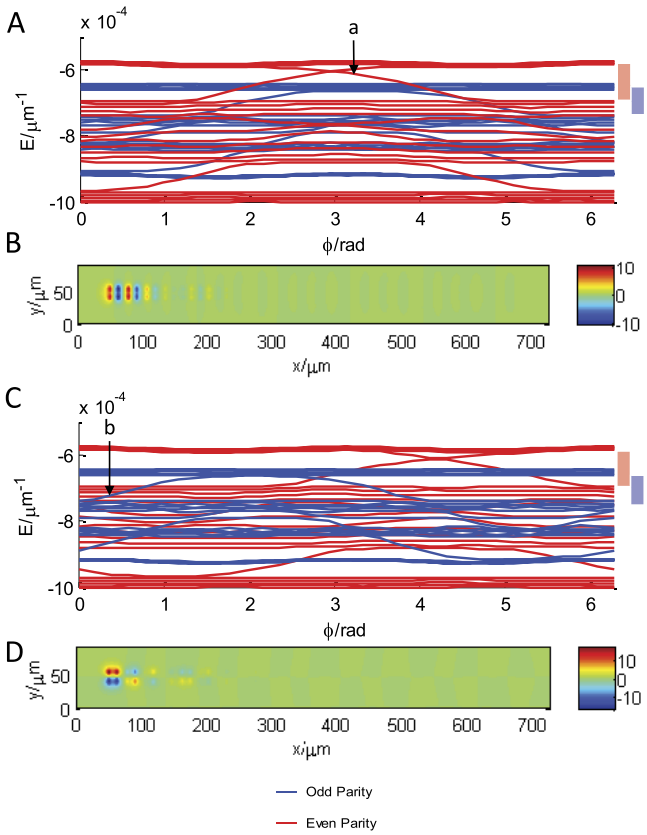

FIG. 4. (a) and (c) show energy spectra for our waveguide chain I and II, respectively. Boundary modes, depicted by "*a*" and "*b*" in (a) and (c), exist in the mini-gap and the corresponding wave functions, as shown in (b) and (d), are localized at the left boundary and possess even and odd parities, respectively. The light red and light blue bar to the right indicate the range of interested mini-gap of the respective parities mapped to Fig. 3(b) of the tight-binding model. A tight-binding model simulation using the same parameters is shown in the supplementary material[60] for comparison.

TABLE I. Parameters in the tight-binding model to describe Fig. 4. The corresponding tight-binding spectrum is shown in Fig. II.2 (supplemental material[60]). The values are fitted from the mapping between the tight-binding model and the continuum simulation.

Parameter	Value
V_0/mm^{-1}	−0.8
λ/mm^{-1}	0.1
$\gamma_{x0}/\text{mm}^{-1}$	−0.275
$\gamma_{y0}/\text{mm}^{-1}$	−0.3
t/mm^{-1}	−0.13
t'/mm^{-1}	−0.062
b	$\sqrt{5}$
M	23
m_0	22 for chain I, 0 for chain II

Next, we focus on energy bands that correspond to $|\psi_\pm\rangle$ bands in our tight-binding model. For both the bands with even (red color) and odd (blue color) parities, they are split into three mini-bands, separated by mini-gaps. Within the mini-gap, boundary modes can exist for both parity bands. Examples of boundary modes are marked by a for even parity bands in Fig. 4(a) (waveguide configuration I) and b for odd parity bands in Fig. 4(c) (waveguide configuration II), both at the left edge of the chain. For these two states, the corresponding wave functions are shown in Figs. 4(b) and 4(d), respectively, from which one can clearly see that both modes are highly localized with a penetration length around twice of the lattice constant. We emphasize that we need to carefully choose the value of ϕ in Fig. 4(a) (Fig. 4(c)), and at that ϕ value, only one boundary mode "a" ("b") at that edge is supported and this is important for the simulations of parity selected time evolution of boundary modes, as well as parity selected charge pump, described below.

We next inject a wave packet into one end of the waveguide chain and study time evolution of wave packets with different parities in this chain by solving the time-dependent Schrödinger equation, Eq. (8), numerically. Details of our simulation are included in the supplementary material.[60] The initial wave packet is chosen to be in Gaussian form, given by

$$\psi_\pm^{\text{ini}}(x,y) = \mathcal{N}\exp\left(-\frac{(x-x_0)^2}{2\sigma_x^2} - \frac{(y-y_0)^2}{2\sigma_y^2}\right) f_\pm(x,y), \tag{9}$$

where $\mathcal{N}$ is a normalization factor, (x_0, y_0) is the center of Gaussian form and chosen to be the center of the first two unit cells. The function f describes the parity of the injected light beam and is chosen to be $f_-(x,y) = e^{ik_x(x-x_0)}$ for even parity mode and $f_+(x,y) = \sin(k_y(y-y_0))$ for odd parity mode. The size of the envelope function is tuned to cover the majority of the mode wavefunction. We inject an even beam $\psi_-^{\text{ini}}(x,y)$ into the waveguide chain I with $\phi = 1.15\,\pi$ (the value of ϕ for the mode "a" in Fig. 4(a)), and the corresponding time evolution is shown in the first row of Fig. 5, from which one can see that the wave packet keeps localized after a long time evolution. In contrast, when we inject $\psi_+^{\text{ini}}(x,y)$ into the same waveguide configuration, the light spreads into the bulk of

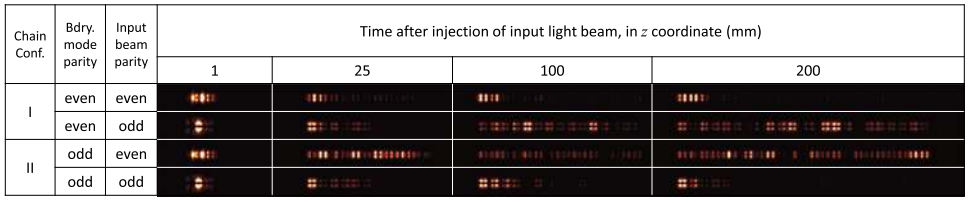

FIG. 5. Numerical simulation of time-dependent evolution for the injection of the light beam $\psi_\pm^{\text{ini}}$ into the waveguide chain configuration I and II. The corresponding boundary mode parities and input beam parities are listed in the second and third column, respectively. Evolution time is expressed in unit of z-direction coordinate. Density profiles for wavefunctions at $z = 1$, 25, 100, and 200 mm are presented. The dark parts in first three columns of the images are cropped.

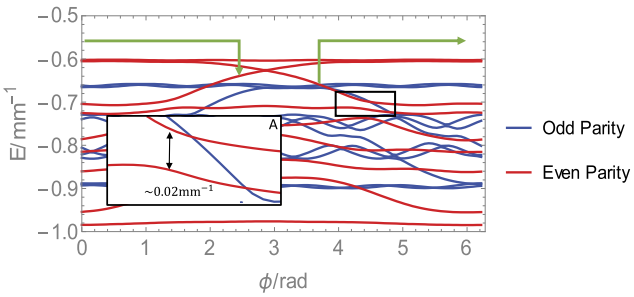

FIG. 6. Energy spectrum for $M = 10, m_0 = 1$ used in the adiabatic pumping. Blue and red colors represent odd and even mirror parities. The green arrow denotes the direction of change of parameter ϕ, crossing the Brillouin zone boundary once. Inset A enlarges the part where the boundary mode enters the bulk. The gap schematically shows the separation between the boundary mode and a nearby bulk mode. To keep the adiabaticity, the changing rate of ϕ should be proportional to the size of this gap.

the waveguide chain, as shown in the second row of Fig. 5. For chain II with $\phi = 0.25\ \pi$ (the value of ϕ for the mode "b" in Fig. 4(c)), the light will get delocalized with initial wave packet $\psi_{-}^{\mathrm{ini}}(x, y)$, but localized with initial wave packet $\psi_{+}^{\mathrm{ini}}(x, y)$, as shown in the last two rows of Fig. 5. Therefore, we conclude that the localization of boundary modes at the boundary sensitively depends on their mirror parities. Therefore, our numerical simulation also provides an approach to probe topological crystalline protection of boundary modes in realistic experiments.

Furthermore, topological transport can also be realized in our system. We may prepare the initial wavefunction at one edge with the corresponding $\phi_i = 1.2\ \pi$. By adiabatically changing the parameter ϕ to $\phi_f = (2 + 0.8)\pi$ where there exists a boundary mode on the other end, we are able to "pump" the light wave packet along the x axis (see the green arrow in Fig. 6). For illustration, we show the evolution of an (instantaneous) eigenstate being pumped from the left to the right edge by artificially requiring the input beam being one edge state localized on the left edge. The chain configuration is similar to chain I (See Table I) with the modification of $M = 10$ and $m_0 = 1$. Here we limit the sample size to better illustrate the pumping process. The corresponding spectrum is shown in Fig. 6, which resembles the one of chain I in Fig. 4.

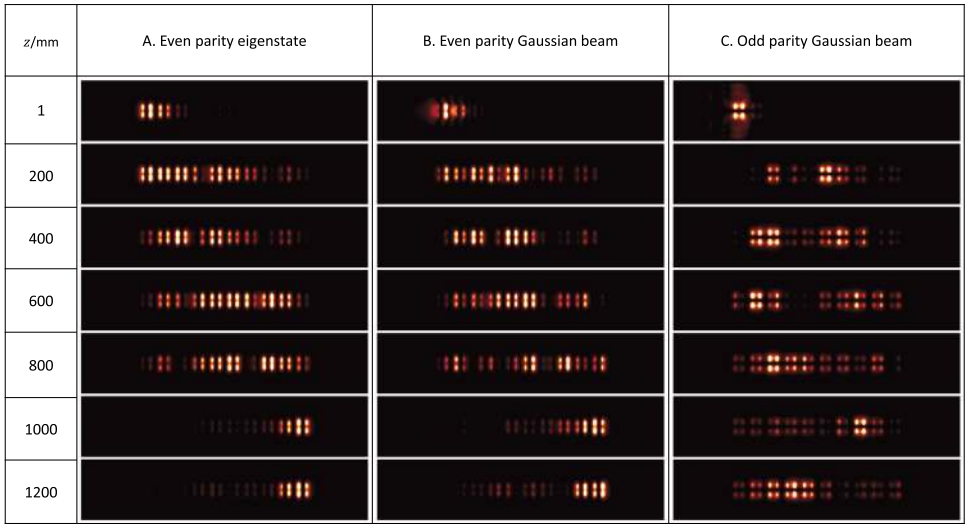

FIG. 7. Numerical simulation of time-dependent evolution for the adiabatic pumping. The three columns correspond to the even mode eigenstate, light beam $\psi_{\pm}^{\mathrm{ini}}$, respectively. The waveguide configuration is same as chain 1 but with $M = 10$ and $m_0 = 1$. Evolution time is expressed in units of z-direction coordinate. Density profiles for wavefunctions from $z = 1$ to 1200 mm are presented, while the parameter ϕ changes from $\phi_i = 1.2\ \pi$ to $\phi_f = (2 + 0.8)\ \pi$ linearly. The system selectively pumps only even wavefunctions, both the eigenstate and the even Gaussian beam, while the odd Gaussian beam gets delocalized into the bulk. To keep the adiabaticity, the evolution time is much longer compared to that in Fig. 5.

The result in Fig. 7(a) is a clear evidence that the optical wavefunction is undergoing adiabatic pumping. This is similar to topological charge pumping (Thouless pumping) in 1D AA model.[52] However, the pumping here depends on the parity of the initial wave packet in our system. In Figs. 7(b) and 7(c), we compare the pumping of initial Gaussian beams with even and odd parity, respectively, in the same waveguide configuration as that in Fig. 7(a). One can clearly see that even-parity beam is almost pumped across the waveguide chain from one end to the other with negligible parts remaining in the bulk of the chain, while the odd-parity beam spreads over the whole chain. This simulation demonstrates the parity-selective charge pump in our system.

DISCUSSION AND CONCLUSION

This proposal aims at a photonic realization of crystalline symmetry protected topological states. We would like to emphasize that the realization in photonic systems is not equivalent to that in electronic systems because of the discrepancy between different topological classifications of bosonic and fermionic systems.[49] Our work on the photonic systems will pave the way to realize other topological crystalline phases, as listed in Table I (the spinless case) in Ref. 49.

Based on a tight-binding model and continuum numerical simulation, we propose an experimental setup of a photonic lattice to realize topological crystalline protection of boundary modes in photonic systems. Numerical simulation also suggests a possible experimental configuration to detect topological boundary modes, in which the edge localization behavior depends on the parities of both the injected wave packets and localized boundary modes. In addition, we would like to emphasize that the two degenerate states realized in our system can also be regarded as "pseudo-spin" and thus provide a natural platform to construct SU(2) Landau levels[72] and spin-orbit coupling in future studies. The fact that the model was simulated with both tight-binding and more experimentally realistic continuum simulations suggests that it can be implemented in a scheme similar to previously realized time-reversal-broken topological phases in photonic lattices. This will open the door to the exploration of topological crystalline protection in interacting systems based on the nonlinear optical response of the ambient medium (giving rise to the nonlinear Schrödinger / Gross-Pitaevskii equation), and entangled quantum walks in such phases (based on injecting entangled photons into the structure). A question of central importance in TCI physics is the question of disorder: since edge state protection is achieved using a symmetry that is easily broken (i.e., crystalline/mirror symmetry) by disorder, what is the nature of the robustness of these states? Will all protection simply break down, or is it preserved in an ensemble-sense? These are fundamental questions where photonics provides a unique and versatile path forward.

ACKNOWLEDGMENTS

We would like to acknowledge helpful discussions with Ling Lu, Marin Soljačić, Rui-Xing Zhang, Jiabin Yu, and Yang Ge. C.-X.L. acknowledges the support from Office of Naval Research (Grant No. N00014-15-1-2675). M.C.R. acknowledges the support of the National Science Foundation under Grant No. ECCS-1509546.

[1] F. Haldane and S. Raghu, Phys. Rev. Lett. **100**, 013904 (2008).
[2] S. Raghu and F. Haldane, Phys. Rev. A **78**, 033834 (2008).
[3] L. Lu, J. D. Joannopoulos, and M. Soljačić, Nat. Photonics **8**, 821 (2014).
[4] Z. Wang, Y. Chong, J. D. Joannopoulos, and M. Soljačić, Phys. Rev. Lett. **100**, 013905 (2008).
[5] Z. Wang, Y. Chong, J. Joannopoulos, and M. Soljačić, Nature **461**, 772 (2009).
[6] R. Umucalılar and I. Carusotto, Phys. Rev. A **84**, 043804 (2011).
[7] M. Hafezi, E. A. Demler, M. D. Lukin, and J. M. Taylor, Nat. Phys. **7**, 907 (2011).
[8] K. Fang, Z. Yu, and S. Fan, Nat. Photonics **6**, 782 (2012).
[9] G. Q. Liang and Y. D. Chong, "Optical resonator analog of two-dimensional topological insulator," Phys. Rev. Lett. **110**, 203904 (2013).
[10] A. B. Khanikaev, S. H. Mousavi, W.-K. Tse, M. Kargarian, A. H. MacDonald, and G. Shvets, Nat. Mater. **12**, 233 (2013).
[11] M. C. Rechtsman, J. M. Zeuner, Y. Plotnik, Y. Lumer, D. Podolsky, F. Dreisow, S. Nolte, M. Segev, and A. Szameit, Nature **496**, 196 (2013).

[12] M. Hafezi, S. Mittal, J. Fan, A. Migdall, and J. Taylor, Nat. Photonics **7**, 1001 (2013).
[13] X.-L. Qi and S.-C. Zhang, Phys. Today **63**(1), 33 (2010).
[14] J. E. Moore, Nature **464**, 194 (2010).
[15] X.-L. Qi and S.-C. Zhang, Rev. Mod. Phys. **83**, 1057 (2011).
[16] M. Z. Hasan and C. L. Kane, Rev. Mod. Phys. **82**, 3045 (2010).
[17] C. L. Kane and E. J. Mele, Phys. Rev. Lett. **95**, 146802 (2005).
[18] B. A. Bernevig and S.-C. Zhang, Phys. Rev. Lett. **96**, 106802 (2006).
[19] J. E. Moore and L. Balents, Phys. Rev. B **75**, 121306 (2007).
[20] L. Fu and C. L. Kane, Phys. Rev. B **76**, 045302 (2007).
[21] R. Roy, Phys. Rev. B **79**, 195322 (2009).
[22] S. Ryu, A. P. Schnyder, A. Furusaki, and A. W. Ludwig, New J. Phys. **12**, 065010 (2010).
[23] A. P. Schnyder, S. Ryu, A. Furusaki, and A. W. Ludwig, Phys. Rev. B **78**, 195125 (2008).
[24] B. A. Bernevig, T. L. Hughes, and S.-C. Zhang, Science **314**, 1757 (2006).
[25] M. König, S. Wiedmann, C. Brüne, A. Roth, H. Buhmann, L. W. Molenkamp, X.-L. Qi, and S.-C. Zhang, Science **318**, 766 (2007).
[26] D. Hsieh, Y. Xia, D. Qian, L. Wray, F. Meier, J. Dil, J. Osterwalder, L. Patthey, A. Fedorov, H. Lin *et al.*, Phys. Rev. Lett. **103**, 146401 (2009).
[27] H. Zhang, C.-X. Liu, X.-L. Qi, X. Dai, Z. Fang, and S. Zhang, Nature Phys. **5**(6), 438–442 (2009).
[28] Y. Chen, J. Analytis, J.-H. Chu, Z. Liu, S.-K. Mo, X.-L. Qi, H. Zhang, D. Lu, X. Dai, Z. Fang *et al.*, Science **325**, 178 (2009).
[29] D. Hsieh, Y. Xia, L. Wray, D. Qian, A. Pal, J. Dil, J. Osterwalder, F. Meier, G. Bihlmayer, C. Kane *et al.*, Science **323**, 919 (2009).
[30] D. Hsieh, Y. Xia, D. Qian, L. Wray, J. Dil, F. Meier, J. Osterwalder, L. Patthey, J. Checkelsky, N. Ong *et al.*, Nature **460**, 1101 (2009).
[31] Y. Xia, D. Qian, D. Hsieh, L. Wray, A. Pal, H. Lin, A. Bansil, D. Grauer, Y. Hor, R. Cava *et al.*, Nat. Phys. **5**, 398 (2009).
[32] C. Liu, T. L. Hughes, X.-L. Qi, K. Wang, and S.-C. Zhang, Phys. Rev. Lett. **100**, 236601 (2008).
[33] C.-Z. Chang, J. Zhang, X. Feng, J. Shen, Z. Zhang, M. Guo, K. Li, Y. Ou, P. Wei, L.-L. Wang *et al.*, Science **340**, 167 (2013).
[34] R. Yu, W. Zhang, H.-J. Zhang, S.-C. Zhang, X. Dai, and Z. Fang, Science **329**, 61 (2010).
[35] V. Mourik, K. Zuo, S. Frolov, S. Plissard, E. Bakkers, and L. Kouwenhoven, Science **336**, 1003 (2012).
[36] L. Fu and C. L. Kane, Phys. Rev. Lett. **100**, 096407 (2008).
[37] A. Das, Y. Ronen, Y. Most, Y. Oreg, M. Heiblum, and H. Shtrikman, Nat. Phys. **8**, 887 (2012).
[38] R. M. Lutchyn, J. D. Sau, and S. D. Sarma, Phys. Rev. Lett. **105**, 077001 (2010).
[39] J. D. Sau, R. M. Lutchyn, S. Tewari, and S. D. Sarma, Phys. Rev. Lett. **104**, 040502 (2010).
[40] J. Alicea, Phys. Rev. B **81**, 125318 (2010).
[41] L. Fu, Phys. Rev. Lett. **106**, 106802 (2011).
[42] J. C. Teo, L. Fu, and C. Kane, Phys. Rev. B **78**, 045426 (2008).
[43] P. Dziawa, B. Kowalski, K. Dybko, R. Buczko, A. Szczerbakow, M. Szot, E. Łusakowska, T. Balasubramanian, B. M. Wojek, M. Berntsen *et al.*, Nat. Mater. **11**, 1023 (2012).
[44] T. H. Hsieh, H. Lin, J. Liu, W. Duan, A. Bansil, and L. Fu, Nat. Commun. **3**, 982 (2012).
[45] S.-Y. Xu, C. Liu, N. Alidoust, M. Neupane, D. Qian, I. Belopolski, J. Denlinger, Y. Wang, H. Lin, L. Wray *et al.*, Nat. Commun. **3**, 1192 (2012).
[46] Y. Tanaka, Z. Ren, T. Sato, K. Nakayama, S. Souma, T. Takahashi, K. Segawa, and Y. Ando, Nat. Phys. **8**, 800 (2012).
[47] P. Jadaun, D. Xiao, Q. Niu, and S. K. Banerjee, Phys. Rev. B **88**(8), 085110 (2013).
[48] C. Fang, M. J. Gilbert, S.-Y. Xu, B. A. Bernevig, and M. Z. Hasan, Phys. Rev. B **88**, 125141 (2013).
[49] X.-Y. Dong and C.-X. Liu, Physical Review B **93**(4), 045429 (2016).
[50] C.-X. Liu, R.-X. Zhang, and B. K. VanLeeuwen, Phys. Rev. B **90**, 085304 (2014).
[51] L. Lu, C. Fang, L. Fu, S. G. Johnson, J. D. Joannopoulos, and M. Soljačić, Nature Phys. **12**, 337–340 (2016).
[52] Y. E. Kraus, Y. Lahini, Z. Ringel, M. Verbin, and O. Zilberberg, Phys. Rev. Lett. **109**, 106402 (2012).
[53] L.-H. Wu and X. Hu, Phys. Rev. Lett. **114**, 223901 (2015).
[54] A. Peruzzo, M. Lobino, J. C. Matthews, N. Matsuda, A. Politi, K. Poulios, X.-Q. Zhou, Y. Lahini, N. Ismail, K. Wörhoff *et al.*, Science **329**, 1500 (2010).
[55] N. Malkova, I. Hromada, X. Wang, G. Bryant, and Z. Chen, Opt. Lett. **34**, 1633 (2009).
[56] C. L. Fefferman, J. P. Lee-Thorp, and M. I. Weinstein, Proceedings of the National Academy of Sciences **111**, 8759–8763 (2014).
[57] C. Poli, M. Bellec, U. Kuhl, F. Montessagne, and H. Schomerus, Nat. Commun. **6**, 6710 (2015).
[58] A. P. Slobozhanyuk, A. N. Poddubny, A. E. Miroshnichenko, P. A. Belov, and Y. S. Kivshar, Phys. Rev. Lett. **114**, 123901 (2015).
[59] A. Blanco-Redondo, I. Andonegui, M. J. Collins, G. Harari, Y. Lumer, M. C. Rechtsman, B. J. Eggleton, and M. Segev, Phys. Rev. Lett. **116**, 163901 (2016).
[60] See supplementary material at http://dx.doi.org/10.1063/1.4953364 for the derivation of mapping to the 2D topological mirror insulator; detailed parameters and relations between the tight-binding model for the purpose of reproducing the results; a standard definition of mirror Chern number in our system.
[61] S. Aubry and G. André, Ann. Isr. Phys. Soc. **3**, 18 (1980).
[62] S. Ganeshan, K. Sun, and S. D. Sarma, Phys. Rev. Lett. **110**, 180403 (2013).
[63] D. R. Hofstadter, Phys. Rev. B **14**, 2239 (1976).
[64] A. Yariv, *Optical Electronics in Modern Communications* (Oxford University Press, 1997), Vol. 1.

[65] D. Christodoulides and R. Joseph, Opt. Lett. **13**, 794 (1988).
[66] H. Eisenberg, Y. Silberberg, R. Morandotti, A. Boyd, and J. Aitchison, Phys. Rev. Lett. **81**, 3383 (1998).
[67] J. W. Fleischer, M. Segev, N. K. Efremidis, and D. N. Christodoulides, Nature **422**, 147 (2003).
[68] T. Schwartz, G. Bartal, S. Fishman, and M. Segev, Nature **446**, 52 (2007).
[69] O. Peleg, G. Bartal, B. Freedman, O. Manela, M. Segev, and D. N. Christodoulides, Phys. Rev. Lett. **98**, 103901 (2007).
[70] M. C. Rechtsman, J. M. Zeuner, A. Tünnermann, S. Nolte, M. Segev, and A. Szameit, Nat. Photonics **7**, 153 (2013).
[71] A. Szameit and S. Nolte, J. Phys. B: At., Mol. Opt. Phys. **43**, 163001 (2010).
[72] Y. Li, S.-C. Zhang, and C. Wu, Phys. Rev. Lett. **111**, 186803 (2013).